Elsevier Editorial System(tm) for Remote Sensing of Environment
Manuscript Draft

Manuscript Number:

Title: Remote sensing of photosynthetic light-use efficiency across two forested biomes: Spatial scaling

Article Type: Full length article

Keywords: PRI; LUE; Light-use efficiency; AMSPEC; Eddy covariance; shadow fraction; GPP; SOA; DF49; Douglas-fir; Aspen; MODIS; MAIAC; Spatial Scaling; Carbon Cycle; Terrestrial Carbon Cycle; LiDAR, Canopy Height Model

Corresponding Author: Dr Thomas Hilker, Ph.D

Corresponding Author's Institution: UBC, Faculty of Forestry

First Author: Thomas Hilker, Ph.D

Order of Authors: Thomas Hilker, Ph.D; Forrest G Hall, PhD; Nicholas C Coops, PhD; Alexei Lyapustin, PhD; Yujie Wang, PhD; Zoran Nesic; Nick Grant; Andrew T Black, PhD; Michael A Wulder, PhD; Natascha Kljun, PhD; Christopher Hopkinson, PhD; Laura Chasmer, PhD

Remote sensing of photosynthetic light-use efficiency across two forested biomes: Spatial scaling

Thomas Hilker[1]
Faculty of Forest Resources Management,
University of British Columbia, 2424 Main Mall, Vancouver, BC, V6T 1Z4, Canada.

Forrest G. Hall
Joint Center for Earth Systems Technology, University of Maryland, Baltimore County
Goddard Space Flight Center, Greenbelt Maryland, 20771, USA, Code 614.4

Nicholas C. Coops
Faculty of Forest Resources Management,
University of British Columbia, 2424 Main Mall, Vancouver, BC, V6T 1Z4, Canada.

Alexei Lyapustin
University of Maryland, Baltimore County, 1000 Hilltop Circle, Baltimore, MD 21250, USA, NASA Goddard Space Flight Center, Code 614.4, Greenbelt Maryland, 20771, USA.

Yujie Wang
University of Maryland, Baltimore County, 1000 Hilltop Circle, Baltimore, MD 21250, USA,
NASA Goddard Space Flight Center, Code 614.4, Greenbelt Maryland, 20771, USA.

Zoran Nesic
Faculty of Land and Food Systems,
University of British Columbia, 2357 Main Mall, Vancouver, BC, V6T 1Z4, Canada

Nick Grant
Faculty of Land and Food Systems,
University of British Columbia, 2357 Main Mall, Vancouver, BC, V6T 1Z4, Canada

T. Andrew Black
Faculty of Land and Food Systems,
University of British Columbia, 2357 Main Mall, Vancouver, BC, V6T 1Z4, Canada

Michael A. Wulder
Canadian Forest Service (Pacific Forestry Centre), Natural Resources Canada, 506 West Burnside Road, Victoria, BC, V8Z 1M5, Canada

Natascha Kljun
Department of Geography, School of the Environment and Society, Swansea University,
Swansea SA2 8PP, UK

Chris Hopkinson
Applied Geomatics Research Group, NSCC Annapolis Valley Campus, 295 Commercial St. Middleton, NS B0S 1P0

Laura Chasmer, CRRC, Wilfrid Laurier University
Cold Regions Research Centre, Wilfrid Laurier University, Waterloo, ON, N2L 3C5, Canada

[1] * corresponding author: Phone: +1 (604) 827 4429, Fax :+1 (604) 822 9106, thomas.hilker@ubc.ca

Abstract

Eddy covariance (EC) measurements have greatly advanced our knowledge of carbon exchange in terrestrial ecosystems. However, appropriate techniques are required to upscale these spatially discrete findings globally. Satellite remote sensing provides unique opportunities in this respect, but remote sensing of the photosynthetic light use efficiency (ε), one of the key components of Gross Primary Production, is challenging. Some progress has been made in recent years using the photochemical reflectance index, a narrow waveband index centered at 531 and 570nm. The high sensitivity of this index to various extraneous effects such as canopy structure, and the view observer geometry has so far prevented its use at landscape and global scales. One critical aspect of upscaling PRI is the development of generic algorithms to account for structural differences in vegetation. Building on previous work, this study compares the differences in the PRI:ε relationship between a coastal Douglas-fir forest located on Vancouver Island, British Columbia, and a mature Aspen stand located in central Saskatchewan, Canada. Using continuous, tower-based observations acquired from an automated multi-angular spectroradiometer (AMSPEC II) installed each site, we demonstrate that PRI can be used to measure ε throughout the vegetation season at the DF-49 stand (r^2=0.91, p<0.00) as well as the deciduous site (r^2=0.88, p<0.00). It is further shown that this PRI signal can be also observed from space at both sites using daily observations from the Moderate Resolution Imaging Spectro-radiometer (MODIS) and a multi-angular implementation of atmospheric correction (MAIAC) (r^2=0.54 DF-49; r^2=0.63 SOA; p<0.00). By implementing a simple hillshade model derived from airborne light detection and ranging (LiDAR) to approximate canopy shadow fractions (α_s), it further demonstrated that the differences observed in the relationship between PRI and ε at DF-49 and SOA can be attributed largely to differences in α_s. The findings of this study suggest that algorithm used to separate physiological from extraneous effects in PRI reflectance may be more broadly applicable and portable across these two climatically and structurally different biome types, when the differences in canopy structure are known.

1. Introduction

Global and spatially continuous estimates of plant photosynthesis are required for a comprehensive understanding of the terrestrial carbon cycle and the determination of CO_2 uptake by plants (Barr et al. 2004). Over the last few decades, eddy covariance measurements of CO_2 exchange between the canopy surface and its surrounding air column have greatly improved our understanding of carbon cycling at the stand level (Baldocchi 2003); however, appropriate techniques are required to upscale these findings to landscape and global scales (Chen et al. 2003; Reichstein et al. 2007). Satellite remote sensing offers unique opportunities in this respect, through provision of a globally continuous parameterization of the land surface at regular time intervals from space (Hall et al. 2005).

Gross primary production (GPP) of green vegetation is proportional to the photosynthetically active radiation (PAR [MJ]) incident upon the canopy at a given time, the fraction of it being absorbed by the green vegetation elements (f_{PAR}) and the efficiency ε [g CMJ^{-1}] with which plants can use this absorbed radiation energy to produce biomass (Monteith 1972, 1977). This efficiency, also known as light-use efficiency, is driven by any of a large number of factors restraining the photochemical reaction process, such as temperature, nutrient and water supply and, as a result, varies greatly in space and time (Field and Mooney 1986). One of the most common methods used for remote sensing of ε is the photochemical reflectance index (PRI) (Gamon et al. 1993; Gamon 1992), a narrow waveband, normalized difference index that relates ε to a xanthophyll-induced absorption feature at 531 nm, which is intimately linked to the biochemical mechanism down-regulating photosynthesis and dissipating excessive radiation energy as heat (Demmig- Adams and Adams 1996). While the relationship between PRI and ε has been proven across a wide range of species (Filella et al. 1996; Gamon et al. 1993; Garbulsky et al. 2008; Penuelas et al. 1995), its generalization to satellite observable scales is challenging, as PRI is also driven by numerous other factors including the sun-observer geometry, soil background reflectance, canopy structure and the ratio of carotenoid to chlorophyll concentration(also referred to as pigment pool size) (Asner 1998; Barton and North 2001; Hall et al. 2008; Hilker et al. 2008a). In addition to the uncertainties existing at the close range, spaceborne observations of PRI are also confounded by atmospheric scattering (Drolet et al. 2005; Drolet et al. 2008; Hilker et al. 2009b). Although these effects can generally be accounted for by modeling the radiative transfer of light through the atmosphere (Vermote and Kotchenova 2008; Vermote et al. 1997), the simplifying assumptions underlying the commonly used, single orbit-based atmospheric correction algorithms, cause uncertainties in the PRI wavebands (Hilker et al. 2009b), whose total change in reflectance between relaxed and photo-inhibited state is in the order of only about 6% (Hall et al. 2008).

Using a tower-mounted, automated multi-angular spectro-radiometer (AMSPEC), Hilker et al. (2008) introduced a technique to separate the extraneous effects from the physiological signal contained in stand level PRI which allowed, for the first time, a temporally continuous remote sensing of ε. Year-round reflectance data were stratified into observations taken under homogenous physiological and atmospheric conditions and the bi-directional reflectance distribution function (BRDF) was determined separately for each stratum. It was then shown that the physiological component of the canopy-level PRI signal was contained in the change of BRDF adjusted reflectance across strata (Hilker et al. 2008a) which were directly linked to changes in the xanthophyll cycle of vegetation (Hall et al. 2008).

At the satellite scale, Drolet et al. (2005) introduced a first spaceborne assessment of ε, using data acquired from the Moderate Resolution Imaging Spectroradiometer (MODIS). A relationship between the normalized difference of MODIS bands 11 and 12 (PRI_{12}) and EC-measured- ε was found when restricting data to backscatter observations (Drolet et al. 2005). Similar studies since confirmed these findings (Drolet et al. 2008; Goerner et al. 2009). Building on the work of Drolet et al. (2005, 2008), Hilker et al. (2009b) used AMSPEC data to "translate" EC-measured ε into a stand-level PRI signal first, which was then compared to MODIS observations after adjusting the viewing geometries of the two sensors. A new, multi-angular implementation of atmospheric correction (MAIAC) algorithm (Lyapustin and Wang, 2009) was used to correct for atmospheric scattering which, for the first time, allowed the use of forward and backward scatter observations. Previously, the atmospheric noise in the MODIS standard product, and an incomplete correction for BRDF effects masked the weaker forward scatter PRI changes with LUE variations. The MAIAC-corrected MODIS PRI markedly enhanced the relationship between MODIS and tower-based observations throughout the year (Hilker et al. 2009b).

One critical aspect for the development of a more generic algorithm that allows remote sensing of ε across the landscape and eventually at global scales, is the study of species and structure related differences in PRI (Gamon et al. 1993). For instance, Barton and North (2001) found that PRI is sensitive to species related differences in leaf angle distribution and leaf area. Similarly, (Gamon et al. 1997) found statistically significant differences in the mean annual PRI across a range of different plant functional types. (Sims and Gamon 2002) found PRI observations to be sensitive to variations in the pigment pool sizes existing across species and over time. In this study, we assess and compare the differences in the relationship between PRI and ε across two forested biomes using data simultaneously acquired at the Douglas-fir (*Pseudotsuga menziesii* var *menziesii* (*Mirb*.) *Franco*) stand and a mature Aspen forest located in Prince Albert National Park, Saskatchewan, Canada. First, we demonstrate that the approach previously used to establish a year round, stand-level relationship between PRI and ε at the Douglas-fir site (hereafter DF-49) (Hilker et al. 2008a) can successfully be applied also at the Aspen stand. Second, tower-borne PRI data acquired at both sites are related to spaceborne observations taken from the MODIS sensor (Hilker et al. 2009b) and the relationships are compared between the two sites. Finally, the differences between the PRI:ε relationships observed at the coniferous and deciduous stand are being investigated and quantified using a LiDAR derived model of the canopy surface to assess mutual shading effects of individual tree crowns. Our results show that the differences in the PRI:ε relationship between the sites can be attributed to differences in canopy shadow fractions (α_s) existing at the coniferous and deciduous stand. Furthermore, we show that the instantaneous derivative of PRI with respect to α_s, computed from multi-angle sensor measurement, can be used to infer instantaneous canopy ε for both the Douglas-fir and Aspen sites using a single functional relation. Our results suggest that multi-angle remote sensing techniques of ε might be species invariant thus applicable across vegetated landscapes without detailed knowledge of vegetation structure and composition.

2. Methods

2.1 Study areas

The DF-49 site is a 61-year old, second-growth coniferous forest located on Vancouver Island, British Columbia, Canada, at 300 m above sea level (49°52'7.8" N, 125°20'6.3" W). The stand consists of 80% Douglas fir, 17% western red cedar (Thuja plicata Donn ex D. Don) and 3% western hemlock (Tsuga heterophylla (Raf.) Sarg.) and is among the most productive in Canada (Morgenstern et al. 2004). The stand density is 1100 stems ha^{-1}, with tree height ranging between 30 and 35 m. The site is located within the dry maritime Coastal Western Hemlock bio-geoclimatic subzone (mean annual temperature ≈8.5˚C), which is characterized by cool summers and mild winters with occasional drought during late summer (Humphreys et al. 2006). The leaf area index (LAI) is 7.3 m m^{-2} (Chen et al. 2006).

The mature Aspen study site, hereafter referred to as Southern Old Aspen (SOA), has been established as part of the Boreal Ecosystem-Atmosphere Study (BOREAS) carried out between 1994 and 1996 and is located in central Saskatchewan (53.62889° N, 106.19779° W, altitude 600 m). The 86-year old stand is situated in the southern ecotone of the western boreal forests (mean annual temperature ≈0.5˚C) and consists of trembling aspen (*Populus tremuloides* Michx) with about 10% of balsam poplar (*Populus balsamifera* L.) and a thick, 2-3 m hazelnut understory (*Corylus cornuta* Marsh) with sparse alder (*Alnus crispa* (Alt.) Pursch) (Barr et al. 2007). A 1998 stand survey found the stem density was 830 stems ha^{-1}, the mean tree height of the overstorey is about 22 m (Barr et al. 2007), and the mean LAI is 2.1 m m^{-2} (Chen et al. 2006).

2.1 Eddy covariance measurements

Continuous, half-hourly fluxes of CO_2 have been acquired at DF-49 and SOA as part of the Canadian Carbon Program (Margolis et al. 2006). Net ecosystem exchange (NEE) was determined as the sum of the half-hourly fluxes of CO_2 and the rate of change in CO_2 storage in the air column between ground and EC measurement level, using a three-axis sonic anemometer-thermometer (Model R3, Gill Instruments Ltd., Lymington, UK, both sites) and a closed-path CO_2/H_2O infrared gas analyzer (LI-6262, LI-COR Inc., Lincoln, NE, USA, both sites) (Barr et al. 2004; Jassal et al. 2007). Incident and reflected PAR [μmol m^{-2} s^{-1}] was measured from upward and downward looking quantum sensors (model 190 SZ and 190SA, LI-COR Inc. at DF-49 and SOA, respectively) above and below the canopy and f_{PAR} was derived at each site from the incident and reflected total PAR measured above and below the canopy, leaf area index, and the solar zenith angle (θ) at the time of measurement (Chen 1996; Chen et al. 2006). Gross primary production (GPP) was determined as the difference between NEE and daytime ecosystem respiration (R_D)(Humphreys et al. 2006) and ε was calculated as (Monteith 1972, 1977)

$$\varepsilon = \frac{GPP}{PAR \times f_{PAR}} \quad (1)$$

2.2 LiDAR data acquisition

Discrete return airborne LiDAR data were acquired at the DF-49 site on August 14th 2008, using a Leica ALS50-II recording up to 4 returns per outbound laser pulse. The sensor pulse rate was 110 kHz, at an approximate flying altitude of 900 m. The estimated GPS accuracy of the sensor was 0.02, 0.03 and 0.05 m in x, y and z, respectively. When both ground and non-ground returns were considered, the dataset had an average density of 3.74 pts m^{-2}. Ground and non-ground returns were separated using a series of algorithms appropriate for the ground topography (Kraus and Pfeifer 1999) and canopy height model was generated at a spatial resolution of 1 m (Fusion v 2.65, USDA, Forest Service). See (Coops et al. 2007) for more details.

A second multiple return (≤ 4) airborne LiDAR data collection was acquired by the Applied Geomatics Research Group, Nova Scotia at the OA site on August 3rd, 2008 using an Optech Inc. (Toronto, Canada) Airborne Laser Terrain Mapper (ALTM) 3100. The survey was configured using a pulse repetition frequency (PRF) of 71 kHz, a flying altitude ranging between 700 m and 800 m, and a scan angle of ±20 degrees from nadir. A 50% flight line swath overlap was used, resulting in a point density of approximately 10 returns per m^2. All multiple return point positions were post-processed relative to a nearby GPS base station located over a survey monument within 30 km of the survey area. Following integration of sensor position, attitude and laser range data, the point cloud data were tiled, outlying points were filtered, a bundle-adjustment or strip-matching procedure was applied to all flight lines, and the 'cleaned' point-cloud was classified into "ground", "non-ground", and "all" returns using TerraScan software (TerraSolid, Finland). Validation flights performed over a previously surveyed airport runway prior to and following the data collection demonstrated that RMS errors in point cloud elevations were within 10 cm. A digital elevation model (DEM) was created from the ground classified returns using a triangulated irregular network (TIN) interpolation procedure. This surface was then subtracted from a digital surface model (DSM) of the all hits returns, which was generated using an inverse distance weighted (IDW) interpolation procedure. The resultant difference surface was a canopy height model (CHM) at a resolution of 1 m grid cell spacing.

2.3 Tower-based spectral observations

2.3.1 AMSPEC II system

Canopy spectra were automatically obtained at both sites using AMSPEC II (Hilker et al. submitted) an enhanced version of AMSPEC (Hilker et al. 2007). The instrument now features a pan-tilt unit which allows the sensor head to be moved at any zenith angle (θ_v) between 43˚ and 78˚ (view azimuth (ϕ_v) between 0 and 360˚, Figure 1). To allow sampling under varying sky conditions, canopy spectra were obtained from simultaneous measurements of solar irradiance and radiance, sampled every 5 seconds from sunrise to sunset at a 10˚ angular step width (horizontally and vertically), thereby completing a full rotation every 15 minutes. The spectro-radiometer used is a Unispec-DC (PP Systems, Amesbury, MA, USA) featuring 256 contiguous bands with a nominal band spacing of 3nm (full width half maximum 10 nm) and a nominal range of operation between 350 and 1200 nm. The upward pointing probe is equipped with a cosine receptor (PP-Systems) to correct sky irradiance measurements for varying solar altitudes. AMSPEC II also allows tracking of satellite orbits (Crawford et al. 1996; Kelso 2007), thereby driving the radiometer probe to mimic the satellite viewing geometry during each overpass at the site of installation (Hilker et al. submitted). While the probe movements are limited by the physical boundaries of the pan-tilt unit especially for higher satellite elevations, the feature can help stabilizing the BRDF models used to match the viewing geometries of satellite and tower-based measurements (Hilker et al. submitted).

Two identical units were built and installed at DF-49 and SOA, respectively. The DF-49 system was installed on May 14, 2009 at a height of 42m (≈10 m above the tree canopy) on an open-lattice type 0.5 m triangular flux-tower. No observations were made for $190° \leq \phi_v \leq 280°$ due to obstruction by the tower. AMSPEC observations at DF-49 include AMSPEC II data sampled between May 14th and October 20th 2009 and older, AMSPEC I data (same radiometer but at a fixed zenith angle of $\theta_v = 63°$) sampled between April 1st 2006-March 31st 2007, and March 17 – October 21st, 2008 (Hilker et al. 2007).

The SOA system was installed on May 26, 2009 at a height of 37 m (≈15 m above the tree canopy) on a 2.9 m double-scaffold tower. The range of azimuth angles obstructed by the SOA tower was $90° \leq \phi_v \leq 180°$. At SOA, AMSPEC II data were sampled between May 26 and November 4th, 2009.

2.3.2 Determining seasonality from phenological camera data

A fundamental difference between the two sites is the seasonal change in phenology at the coniferous and deciduous stand. While the evergreen DF-49 stand is driven by a temperate climate, with tree growth occurring throughout year (Morgenstern et al. 2004), the deciduous stand is subject to distinct seasonality and the growing season is determined by spring green-up and leaf senescence in fall. The phenological state of deciduous canopies exerts a major control on spatial and temporal patterns of GPP (Richardson et al. 2007), and as a result, seasonal changes in the canopy were expected to greatly affect the spectral observations sampled at SOA (Kodani et al. 2002). Additionally, reflectance observations in the spring and late fall were expected to be strongly affected by soil background effects the reflectance of non-photosynthetically active parts of the canopy. In this study we focus on the spatial aspects of scaling PRI, SOA observations were restricted to the relatively stable growth period during summer, while seasonal and temporal changes will be discussed in a second, forthcoming study.

One of the improvements implemented in AMSPEC II is a webcam system that is installed in parallel to the downward pointing probe and automatically samples an image with every spectrum that is observed by the radiometer (Figure 1) (Hilker et al. submitted). This system was used to track the phenological changes in the plant canopy by quantifying the divergence of the red and the blue channel from the brightness observed in green channel of the camera (Richardson et al. 2007):

$$2G\_RB_i = 2\mu_G - (\mu_R + \mu_B) \qquad (2)$$

where μ_G , μ_R and μ_B are the camera observed brightness values (raw DN) in the green, red and blue channel, respectively. Richardson et al. (2007) introduced an approach to define the seasons in deciduous vegetation by fitting a sigmoid function to the brightness values observed in $2G\_RB_i$ and using its inflection points to mark the beginning and end of the season. In this study, we adapted the method of Richardson et al. (2007) to the slightly more complex patterns found at SOA which are determined by an earlier green-up of the Hazelnut understorey and a secondary green-up of the Aspen overstorey (Barr et al. 2004; Griffis et al. 2004). As a result, a 4th order polynomial rather than a sigmoid was selected to fit the $2G\_RB_i$ observations throughout the observation period and null and inflection points were determined using its first, second and third derivative.

As the webcam observations are also affected by directional and sun illumination effects, one observation was extracted per day (around solar noon) at a fixed viewing direction to minimize the BRDF effects on the camera data. ϕ_v was selected to observe an intermediate amount of shadow within the canopy ($\phi_v = 65°$) while θ_v was set to a off-nadir direction to minimize potential background reflectance effects ($\theta_v = 73°$) (Richardson et al. 2007).

2.3.2 Separating directional and physiological effects on PRI reflectance

The physiological signal contained in multi-angular, canopy-level PRI observations can be separated from extraneous effects when stratifying data into homogenous conditions with respect to the physiological and atmospheric conditions under which they were observed (Hilker et al. 2008a). Within each stratum, the BRDF of PRI can then be modelled as the linear combination of isotropic, geometric and volumetric scattering components (Hilker et al. 2008a; Roujean et al. 1992):

$$PRI(\theta_v, \theta_s, \Delta\phi) = k_i + k_g F_g(\theta_v, \theta_s, \Delta\phi) + k_v F_v(\theta_v, \theta_s, \Delta\phi) \quad (3)$$

where θ_s and $\Delta\phi$ are the view zenith and relative azimuth angle between sun and observer, respectively; k_i, k_g and k_v are the isotropic, geometric and volumetric scattering coefficients, and F_g and F_v represent the geometric and volumetric scattering kernel functions, respectively.

The physiological status of the canopy was determined at SOA and DF-49 using EC-measured ε and the atmospheric conditions were assessed by modelling the clear-sky solar irradiance as a function of θ_s and comparing it to the irradiance measured by AMSPEC at a given time (Hilker et al. 2009a). Observations were stratified in steps of 0.1 $gCMJ^{-1}$ and 10^{th} percentiles of potential sky irradiance, respectively (Hilker et al. 2008a). Geometric and volumetric scattering were modelled at both sites using the Li-Sparse (LS) and Ross-Thick (RT) kernels based on a geometric-optical approach of (Li and Strahler 1985) and the radiative transfer theory of (Ross 1981).

2.4 MODIS data acquisition and atmospheric correction

Daily level 1B (L1B) at-sensor radiances (Collection 5) on board the EOS-Aqua and Terra spacecrafts were acquired for the DF-49 and SOA from the Land Processes Distributed Active Archive Center (LPDAAC) (data portal: https://lpdaac.usgs.gov) for all clear days during the study period and atmospherically corrected using MAIAC (Hilker et al. 2009b; Lyapustin and Wang 2009). The MAIAC algorithm is based on multi-orbit retrievals of calibrated top-of-atmosphere reflectance to simultaneously retrieve atmospheric and surface reflectance parameters, such as aerosol optical thickness (AOT), spectral regression coefficient (SRC) and spectral surface BRDF (Lyapustin and Wang 2005). The time series approach of MAIAC, which directly retrieves surface BRF from measurements, has been shown to yield significantly enhanced relationships between spaceborne and tower-measured PRI as compared to conventional atmospheric correction approach based on a single-orbit data and Lambertian assumption (Hilker et al. 2009b).

MODIS observes the land surface under different viewing geometries, and consequently, the spatial extent of the pixels, or "footprint" varies with each overpass. In order to simplify the handling of MODIS observations, MODIS data are routinely "gridded" to 1 x 1km raster based on a forward and inverse mapping approach which includes the spatially weighted reflectance of adjacent MODIS pixels (Wolfe et al. 1998). While this process greatly simplifies data handling, it also introduces uncertainties to the surface reflectance as the spatial origin of a reflectance measurement becomes less well defined (Tan et al. 2006). In order to assess these uncertainties on PRI reflectance at the two sites, two types of MODIS observations were processed and compared in this study, the gridded 1 km standard product and non-gridded (swath) data (Hilker et al. 2009b).

2.4.1 Adjusting the viewing geometries of MODIS and AMSPEC

One advantage of using the tower-measured PRI observations rather than comparing EC-measurements to MODIS spectra directly, is the possibility to adjust the differences in viewing geometry between the two sensors (Hilker et al. 2009b). Retrieval of accurate BRDF for PRI wavebands from MODIS is difficult, as multiple orbits are required to obtain a sufficient number of different sun-observer geometries, during which the canopy reflectance may change as a result of xanthophyll induced changes in PRI_{12} (Hilker et al. 2008a). AMSPEC completes a full sweep of the forest canopy every 15 minutes. During this time period, the physiological status of the canopy is assumed to be constant (Hilker et al. 2009b). Half-hour observations (±15 minutes from peak elevation of the satellite) were extracted from AMSPEC data during each MODIS overpass at the SOA and DF-49 site and a separate BRDF was modelled for each overpass using the Roujean approach (Eqn. 3) (Hilker et al. 2009b).

MODIS features a band centered at 531 nm (Band 11) which is sensitive to xanthophyll detection, but lacks a suitable reference band at 570 nm (Gamon et al. 1992). This reference band may, however, be substituted using MODIS band 12, a narrow reflectance band centered at 551 nm (Drolet et al. 2005; Drolet et al. 2008; Hilker et al. 2009b). The MODIS-based PRI (PRI_{12}) is defined as (Drolet et al. 2005)

$$PRI_{12} = \frac{\rho_{11} - \rho_{12}}{\rho_{11} + \rho_{12}} \quad (4)$$

where ρ_{11} and ρ_{12} is the reflectance of MODIS band 11 and 12, respectively. In order to make AMSPEC observations more comparable to MODIS, AMSPEC derived spectra were resampled to simulate the 10 nm resolution of the MODIS bands 11 and 12 using the arithmetic mean of the corresponding spectroradiometer wavelengths and PRI_{12} observations were derived also from AMSPEC data.

2.2 Estimation of canopy shading

Under conditions where photosynthesis is limited by factors other than light, sunlit parts of the canopy are exposed to more excessive radiation energy than those shaded by other vegetation elements. Hall et al (2008) showed that under these conditions, canopy level PRI is strongly dependent on α_s, and that the directional changes observed in PRI at a given half hour interval can be attributed almost entirely to changes in α_s (Hall et al. 2008). The same study also showed that the slope of the relationship between α_s and PRI ($\Delta\alpha_s\ \Delta PRI^{-1}$) changes as a function of ε and that PRI shows no variation with α_s when photosynthesis is not down-regulated (Hall et al. 2008). As a result, the instantaneous derivative of PRI with respect to α_s can be used to infer canopy light-use efficiency. The rate of change in $\Delta\alpha_s\ \Delta PRI^{-1}$ should be invariant to species related differences between PRI and ε because Hall et al. (2008) showed theoretically and empirically that $\Delta\alpha_s \Delta PRI^{-1}$ is invariant to non-photosynthetically active canopy elements. These elements, however, are a major driver of spectral differences observed between species.

One simple way to approximate α_s at least under clear sky conditions is using a hillshade algorithm (Hais and Kucera 2009) based on a CHM such as available from LiDAR. While the method takes into account only the mutual shading of tree crowns, Hilker et (2008b) has shown it may still be used to derive realistic estimates of α_s incident upon a canopy at a given time. First, the portions of the canopy visible to AMSPEC were determined by means a viewshed (Kim et al. 2004) applied to the LiDAR derived CHM at SOA and DF-49. Second, a hillshade was applied to model illumination conditions of the visible parts of the canopy areas based upon slope, exposition derived from the CHM and θ_s and ϕ_s at the time of observation. The instantaneous field of view of AMSPEC was approximated as an ellipse given by θ_v and ϕ_v and the height of installation above canopy (h). For each AMSPEC observation, α_s was determined as:

$$\propto_s = 1 - \frac{\sum_1^n \kappa}{n_{(\theta_v,\phi_v)}} \qquad (5)$$

where κ is the modelled brightness of a visible pixel in the hillshade raster (scaled between 0 and 1) and $n_{(\theta_v,\phi_v)}$ is the total number of visible pixels contained in the field of view of AMSPEC at a given time.

One limitation of this LiDAR derived assessment of α_s is that it can only be applied under clear sky conditions (Hilker et al. 2008b) as the model does not account for diffuse sky radiation. In order to assess species related changes between PRI and ε, AMSPEC data were extracted from the two clearest days of each month (as determined by the sum of total daily PAR measured at each site) and used to determine ΔPRI $\Delta\alpha_s^{-1}$ for each 15 minute interval of these days.

3. Results

Figure 2 shows daily estimates of vegetation green-up and leaf-down observed by AMSPEC's webcam system during the 2009 study period. The seasonal dynamics in the $2G\_RB_i$ were much stronger at the Old Aspen site (Figure 2A), compared to the DF-49 site, were almost no changes canopy greenness were observed (Please note that gap in Figure 2B is due to an instrument downtime at DF-49 between DOY

197 and DOY 231). The 4^{th} order polynomial function selected to quantify the seasonal changes at SOA fitted the camera observations well (r^2=0.72, p<0.01). The minimum camera measured $2G\_RB_i$ at this site was observed at around DOY 175. Up until then, the camera data showed a decreasing trend. After DOY 175, the webcam observed a substantial green-up of the canopy, which peaked at around DOY 280. Using null and inflection points of the polynomial function shown in Figure 2A, analysis of AMSPEC observations at SOA was restricted to DOY 175 - 308. Given the little variation in canopy greenness observed at DF-49, all available spectra were used at this site.

The relationship between EC-measured ε and AMSPEC observed, BRDF adjusted PRI and PRI_{12} is given in Figure 3. Figure 3A shows the PRI:ε correlation observed at SOA (DOY 175 - 308), the corresponding observations made at the DF-49 site (all 3 years) are presented in Figure 3B. PRI for the sunlit and shaded part of the canopy is shown (daily averages). At both sites, a highly significant, non-linear relationship existed between AMSPEC measured PRI and ε (r^2=0.88 and r^2=0.91 for SOA and DF-49, respectively (sunlit canopy), p<0.00). At SOA, ε measurements ranged between 0 and 1.8 $gCMJ^{-1}$ while PRI measurements, after being adjusted to a common sun-observer geometry, ranged between $-0.07 \leq PRI \leq -0.02$. At the same time, the maximum ε-value observed at DF-49 was 2.5 $gCMJ^{-1}$ while the spectral measurements varied between $-0.08 \leq PRI \leq -0.02$. The mean coefficient of determination for the BRDF models acquired across all strata was r^2=0.79 and r^2=0.73 (p<0.00) for SOA and DF-49, respectively; the standard deviation in both cases was σ=0.15. Figure 3C and D show the correlation between AMSPEC observed PRI_{12} and EC-measured ε at SOA and DF-49, respectively. PRI_{12} exposed a similarly significant correlation to ε than PRI (Figure 3A and B), the data range,however, was smaller (Figure C and D) and differences between sunlit and shaded parts of the canopy were less prominent.

The results for upscaling tower-based PRI_{12} observation to satellite levels are presented in Figures 4 to 6. Figure 4 shows a BRDF model established from AMSPEC derived PRI_{12} reflectance during one MODIS overpass (spacecraft noon ± 15 minutes) as an example. The model presented in Figure 4A shows observations made at SOA, Figure 4B shows data acquired at DF-49. The x and y-axis in each figure represent the planar coordinates (origin=tower) of the AMSPEC observations (computed from θ_v and ϕ_v and h), the z-axis shows the corresponding ρPRI_{12} value. The black dots represent the actual PRI_{12} measurements of the canopy (for this example: n=203 at SOA and n=184 at DF-49), while the black lines show the residuals to the fitted BRDF-surface. Overall, the semi-empirical reflectance models described the directional changes in tower measured PRI_{12} during the MODIS overpasses well. The average coefficient of determination was r^2=0.93, σ=0.03 (SOA) and r^2=0.98, σ=0.05 (DF49) (p<0.00). The red dots in Figure 4A and 4B represent the PRI_{12} observations taken by AMSPEC in "satellite tracking mode" (here tracking the flight path of EOS-TERRA, both figures). The yellow dot in Figure 4A (blue dot in Figure B) represents the corresponding zenith and azimuth angle of the related MODIS observation. The different colors of the fitted reflectance surface were used to illustrate the shape of the BRDF model.

Figure 5 shows a comparison of the AMSPEC derived, BRDF adjusted MODIS-like PRI based on bands 11 and 12 and PRI from the actual MODIS observations of the same wavelengths (non-gridded observations, Aqua and Terra spacecrafts combined). The measurements taken at SOA are presented in Figure 5A, Figure 5B illustrates the reflectance observed at the DF-49 site. While some differences were found in the absolute reflectance measured by MODIS and AMSPEC (Figure 5A), a significant relationship between MODIS band 11 and 12 and AMSPEC observed band 11 and 12 existed at both research sites (r^2=0.57 (SOA, Band 11), r^2=0.61 (SOA, Band 12), r^2=0.58 (DF-49, Band 11), r^2=0.62 (DF-49, Band 12); p<0.01). A strong correlation also existed between the PRI_{12} measurements of AMSPEC and MODIS at SOA and DF-49 (Figure 6, data from the Aqua and Terra spacecrafts combined). Figure 6A and B shows AMSPEC PRI_{12} observed at SOA compared to PRI_{12} sampled by MODIS using swath data(Figure 6A) and the gridded reflectance product (Figure 6B). Only little difference was found in the strength of the regression of these two datasets (r^2=0.63 and r^2=0.60 for swath and gridded data, respectively; p<0.01).

Highly significant relationships between AMSPEC PRI_{12} and MODIS PRI_{12} were also found for the DF-49 site. As with the Old Aspen site, only little differences were observed in the significance of the regression when using swath (Figure 6C) and gridded reflectance data (Figure 6D) (r^2=0.54 and r^2=0.51 for swath and gridded data, respectively; p<0.01). However, MODIS observations sampled at $\theta_v > 45^\circ$ were excluded from this dataset as previous research (Hilker et al., 2008b) has shown that owing to the increased pixel size at larger off-nadir angles, MODIS PRI_{12} will be confounded by observations of clear-cuts and other non-forested elements.

Figure 7 shows the LiDAR derived CHM observed at SOA (Figure 7A) and DF-49 (Figure 7B). The extent of each raster approximates the largest possible viewing area of AMSPEC at each site ($\theta_v = 78°$). The respective towers are located in the center of each CHM. Notable differences can be observed in the structure of the canopy surface shown in Figure 7A and B with likely implications for α_s estimated at DF-49 and SOA. The colors illustrate the differences in height, the larger gaps visible in Figure 7A are due to bogs found at the SOA site. Figure 8 gives an example of a hillshade model used to determine α_s as a function of the solar position. Figure 8A represents a hillshade modelled from observations made at the Old Aspen site; Figure B shows the corresponding model for DF-49. Areas invisible to AMSPEC (=n.v.) have been eliminated from both hillshade raster by means of the viewshed algorithm. The solar geometry is identical in both examples ($\theta_s = 45°, \phi_s = 170°$), the approximate instantaneous field of view of one AMSPEC observation ($\theta_v = 78°, \phi_v = 225°$) has been illustrated as a superimposed ellipse (Figure 8A and B). While the majority of the canopy was visible at shorter ranges from the tower (<30m), the lower elements of more distant canopy surface areas were increasingly hidden behind other canopy parts and therefore no longer visible AMSPEC. The decrease in visible canopy area with distance from the tower area was rapid especially at the DF-49 site where the triangular crown shape allowed a view only of the tree tops at greater distances from the tower. Figure 9 shows the relationship between AMSPEC observed PRI reflectance and LiDAR estimated α_s during one radiometer sweep (15 minutes) observed under clear sky conditions. Both sites showed a strong linear correlation between PRI and α_s, which was however, more significant at DF-49 (Figure 9B) than at SOA (Figure 9A). The range of α_s between reflectance hotspot and darkspot was about three times bigger at DF-49 than at the SOA site. Both examples chosen in Figure 9 were sampled under similar physiological conditions (ε= 0.45 $gCMJ^{-1}$), roughly an hour before solar noon. Figure 10 shows $\Delta PRI\ \Delta\alpha_s^{-1}$ as a function of EC-measured ε acquired during clear days at DF-49 and SOA, respectively. At both sites, a strong logarithmic relationship was found between $\Delta PRI\ \Delta\alpha_s^{-1}$ and ε. The solid line shows the regression between $\Delta PRI\ \Delta\alpha_s^{-1}$ and ε at the DF-49 site, the dashed line corresponds to the data acquired at SOA. The gray areas correspond to the 95% confidence interval around both regressions. Both regressions are falling within the 95% confidence interval of each other.

4. Discussion

This study compared stand and satellite-scale assessments of PRI and PRI_{12} across two climatically and structurally different forested biomes. The webcam-based approach of Richardson et al (2007) was successfully used to quantify plant phenology and allowed a more objective selection of the study periods at DF-49 and SOA. While the focus of this study was on spatial scaling of PRI and PRI_{12}, a separate study will address potential seasonal changes in the ε:PRI relationship. For instance, the ratio of photosynthetic to non-photosynthetic material is expected to be important driver of canopy level ε (Hall et al., 2008) especially at SOA, were C-uptake early in the year is expected to be driven largely by changes in springtime phenology and leaf green-up (Barr et al. 2004; Richardson et al. 2009). While only one camera position was used in this study to minimize the directional and background effects (Richardson et al. 2007), the multi-angular view of the webcam can potentially provide more information in this respect, as for instance the understorey should be more visible from smaller zenith angles, thus providing more prominent features in $2G\_RB_i$ value earlier in the year (Figure 2A, DOY<180).

At both sites, a strong, non-linear relationship existed between PRI and ε and PRI_{12} and ε throughout the study period (Figure 3). This is an important finding as it demonstrates that the same method to separate physiological and directional effects in PRI is applicable across two structurally and climatically very different forest stands. This finding may also point towards a more generic application of this algorithm, at least in forested biomes, as numerous other studies have demonstrated the principal relationship between PRI and ε (Gamon et al. 1993; Gamon et al. 1997; Penuelas et al. 1997) at the leaf and stand-level scales.

While the PRI measurements under conditions were photosynthesis is not down-regulated (high ε) is similar at SOA and DF-49 (Figure 3A and 3B), the Douglas-fir dominated stand exhibited lower PRI-values under situations where ε is low. Similarly, the PRI_{12} measurements shown in Figure 3C and D are higher at the DF-49 site than at SOA when photosynthesis is less limited by ε. This is consistent with the lower amount of canopy shading observed at SOA (Figure 7,8) and also agrees with the results found in Figure 9 and 10. The difference between sunlit and shaded PRI was more distinct at the DF-49 site than at SOA, which is consistent with the larger range in α_s found at the coniferous site.

Figure 4 demonstrated the suitability of the Li-Sparse and Ross-Thick kernels to model the AMSPEC PRI_{12} reflectance during a half hour interval at SOA and DF-49, thereby allowing a directional adjustment of the spectral observations to MODIS reflectance. The greater range of view zenith angles provided by AMSPEC II compared to the prototype version (Hilker et al. 2007) allowed a greater stability of the BRDF model with respect to predicting changes in PRI at as a function θ_v. This is critical especially when adjusting AMSPEC's geometry to that of satellite data, which, at least for high satellite elevations, cannot be accomplished through direct measurements alone. Also, direct comparisons of measurement taken under identical viewing geometries is not necessarily desirable as 1) soil background reflectance effects may confound AMSPEC observations taken at small zenith angles and 2) a modelled reflectance based on several hundred observations obtained from different locations around the tower can provide a more realistic representation of the stand level reflectance, which is especially critical when scaling to moderate resolution sensors such as MODIS.

Only small differences were found in the significance of the relationship between PRI and ε and PRI_{12} and ε at both sites. This is consistent with previous studies (Drolet et al. 2005; Drolet et al. 2008; Gamon et al. 1992; Hilker et al. 2009b; Middleton et al. 2009) and confirms the use of 551nm as a possible alternative to the commonly used reference wavelength at 570 nm. The comparison between MODIS and AMSPEC derived bands 11 and 12 presented in Figure 5 demonstrates the significant correlation between satellite data and BRDF corrected AMSPEC observations and also confirms the findings in Figure 4, which showed the suitability of the selected LSRT model to adjust directional differences between AMSPEC and MODIS reflectance during a half hour interval. The results shown in Figure 5 are also a rigorous assessment of the quality of MAIAC used to correct for atmospheric effects in MODIS band 11 and 12 (Lyapustin and Wang 2009; Lyapustin 2005) as they demonstrate that MAIAC allows a direct comparison not only of the normalized difference between two bands (Figure 6), but also of absolute reflectance. It should be noted, however, that there are differences in brightness observed by AMSPEC and MODIS at the SOA site (Figure 5A, 6A-B). One possible explanation could be variations in atmospheric conditions, as the BRDF measured by AMSPEC does also include diffuse illumination components, which will vary as function latitude because of differences in path length through the atmosphere.

The results shown in Figure 6 confirm previous findings from the DF-49 (Hilker et al. 2009b) and SOA site (Drolet et al. 2005; Nichol et al. 2000) and demonstrate that spaceborne assessments of ε are possible at least across these two biomes. The data shown in Figure 6 include forward and backscatter observations from the Aqua and Terra spacecrafts combined. This is a significant advancement from the initial results found at SOA (Drolet et al. 2005; Drolet et al. 2008) and underlines the need for a careful consideration of atmospheric and directional impacts on PRI reflectance, which can confound the subtle changes in reflectance induced by physiological changes of the canopy. Almost no differences were found in strength of the correlation between AMSPEC and MODIS observed PRI_{12} reflectance when considering gridded or swath data. This result was expected for SOA as this stand is quite large and homogeneous due to its location inside Prince Albert National Park. As a result, not many changes are to be expected in the neighbouring pixels around the tower. From the experiences of earlier studies (Hilker et al. 2009b) MODIS observations sampled at $\theta_v > 45^{\circ}$ were excluded from the analysis of DF-49 data, which effectively reduced also the origin of the pixels to a smaller area around the tower thereby minimizing the effects of surrounding harvesting activities and clearcuts.

The results shown in Figure 7 and 8 demonstrate the notable differences in canopy shading observed at SOA and DF-49. The hillshade model used in this study was a simple, yet effective proxy of the daily and seasonal cycles in canopy illumination (Hilker et al. 2008b) (Figure 9). It should be noted that the hillshade approach only accounts for mutual shading effects and is therefore only an approximation of the radiation regime at a given time (Hilker et al. 2008b). Additionally, the model does not account for diffuse radiation conditions, and as a result, can only be used under clear sky conditions (One possible approach to extend this method for observations made under cloudy conditions would be to weight the model by the proportion of direct to diffuse irradiance, this is, however, of less interest when validating spaceborne observations). Consequently, this technique should not be considered as an absolute measure of canopy shading, it does, however, previous results have confirmed that it still yields realistic observations of the relative change in α_s (Hall et al. 2008; Hilker et al. 2008b). The results shown in Figure 9A and B are consistent to those shown in Hall et al (2008) and demonstrate the dependency of PRI on α_s during one radiometer sweep at DF-49 and SOA. While significant relationships existed at both study areas, the correlation was stronger at the DF-49 site, which is consistent with the fact that canopy shading is much more predominant in the coniferous than at the deciduous stand. The impact of canopy shading on the stand level radiation regime can also be observed when comparing the range of shadow fractions during one radiometer sweep at SOA and DF-49 (Figure 9).

5. Conclusions

The slope of the relationship between α_s and PRI ($\Delta\alpha_s\Delta PRI^{-1}$) is a very similar logarithmic function of ε (Figure 10) for both sites. The parameters of the two functions do not differ significantly, suggesting that one function can describe two very different vegetation communities, in two very different climates. This is a key finding of this study. First, it confirms that the changes in PRI reflectance at SOA and DF-49 were both driven by physiological changes in the canopy rather than extraneous effects, as demonstrated in the inference framework introduced in Hall et al. (2008). Secondly, it can be concluded from Figure 10 that when viewing the canopy at one angle, as is the case with MODIS, the differences observed in the relationship between PRI and ε at DF-49 and SOA (Figure 4) can be attributed mainly to differences in the canopy structure and shadow fraction. This finding is consistent also with previous studies (Barton and North 2001; Sims and Gamon 2002) and emphasizes the effect of canopy structure on PRI (Hall et al. 2008; Middleton et al. 2009). It shows that single date remote sensing of ε at a single view angle will need to take into account the ratio of photosynthetically active to non-photosynthetic canopy elements, and shadow fraction.

Importantly, the study shows that instantaneous spectral measurements of a canopy at multiple view angles, which are possible using a sensor viewing the canopy along track, as the Chris sensor aboard the Proba platform, could measure both α_s (using visible and NIR bands with mixture decomposition as in Hall et al. 1995) and PRI (using the 531 and 570 nm bands for the different view angles). Along any orbital track an instantaneous estimate of $\Delta\alpha_s\Delta PRI^{-1}$ could then be computed for each pixel in the scene, hence canopy ε could be inferred with a functionally invariant logarithmic relationship across divergent biomes. Adding the NDVI bands to such a sensor to measure f_{PAR} could provide a direct estimate of GPP. In the same way our results show that use of an AMSPEC like instrument suite atop a tower, can directly measure LUE, f_{PAR} and GPP as an adjunct to eddy-correlation measures of NEE and NPP. The advantage of the AMSPEC approach is that it measures GPP directly without the need for measuring respiration. As a result, differencing AMSPEC measures of GPP and eddy-correlation measures of NPP could provide an independent means for inferring respiration without resorting to measurements of night time fluxes (Jassal et al. 2007).

We therefore propose a field campaign including multiple AMSPEC- like instruments to compare continuous PRI measurements and EC-flux data thereby helping to calibrate coarser scale observations to tower-based measurements and assessing the potential for a generic model of PRI across different vegetation and land-cover types.

5. Acknowledgements

We would like to thank Dominic Lessard, Andrew Hum and Rick Ketler from UBC Faculty of Land and Food Systems (LFS) for their assistance in technical design, installation, and maintenance of AMSPEC II. This research is partially funded by the Canadian Carbon Program, the Natural Sciences and Engineering Research Council of Canada (NSERC) and BIOCAP, and an NSERC-Accelerator grant to Dr. Coops. The work of Drs. Lyapustin and Wang was supported by the NASA Terrestrial Ecology Program (Dr. Wickland). Acquisition of the LiDAR data at SOA was supported by NERC (Natural Environment Research Council, UK) grant number NE/G000360/1.

Figures

Figure 1: In-situ photograph of AMSPEC II taken at the Old Aspen site. The system features a pan-tilt unit which allows the sensor head to be moved at any zenith angle between 40 and 78˚ at a view azimuth between 0 and 360˚. The upward looking sensor features a cosine diffuser to correct for varying solar altitudes. Canopy reflectance is determined from solar irradiance and canopy radiance. A webcam picture is automatically taken with every spectrum that is sampled. An identical system has been installed at the DF-49 site.

Figure 2A-B: Estimate of the canopy phenology as observed from AMSPEC's webcam (Richardson et al., 2007). Figure 2A: Spring green-up and leaf down of the Old Aspen site as estimated from 2G_RBi (θ_v=73˚, ϕ_v=65˚). Green-up and leaf-down were quantified using null and inflection points of the polynomial fit. The missing data is due to a downtime of AMSPEC at DF-49 between DOY 197 and 231.

Figure 3A-B: Relationship between AMSPEC-observed PRI and EC-measured ε for hotspot and darkspot reflectance (sunlit and shaded components of the canopy, averaged to daily observations). The SOA site is shown in Figure 3A, Figure 3B represents the PRI- ε relationship at DF-49. Figure 3 C-D: Relationship between AMSPEC -observed PRI_{12} and EC-measured ε at SOA (3C) and DF-49 (3D).

Figure 4A-B: Example of a BRDF model during one MODIS overpass (spacecraft noon ± 15 minutes). Figure 4A shows data from SOA Figure 4B is based on observations taken at DF-49. The x and y-axis represent the planar coordinates (origin=tower), the z axis represents the ρPRI_{12} value at this location.

The black dots represent the actual ρPRI_{12} measurements observed by AMSPEC, the black lines show the residuals to the fitted surface. The red dots are the PRI observations taken by AMSPEC while tracking the flight path of EO-TERRA. The yellow dot (blue dot in Figure B) represents the corresponding zenith and azimuth for the actual MODIS observation. The green dots in Figure 4A represent AMSPEC observations taken with $\theta_z = \theta_v$. No solar tracking was done during this overpass at DF-49 as θ_i exceeded the range of observable θ_z.

Figure 5A-B: Comparison of AMSPEC observed, BRDF adjusted MODIS bands 11 and 12 and MODIS observed reflectance at Band 11 and 12 (2009 data, Aqua and Terra combined). Figure 5A shows observations taken at SOA, Figure 5B shows the reflectance observed at DF-49. The second y-axis for MODIS Band 12 was introduced for illustration purposes.

Figure 6A-D. Comparison between AMSPEC observed, BRDF adjusted PRI_{12} and MODIS PRI_{12}. Figure 6A and B show the results for non-gridded (swath) data and gridded data, observed at SOA Figure 6C and D show the corresponding results for the DF-49 site

Figure 7A-B: LiDAR derived canopy surface model (CSM) observed at SOA (A) and DF-49 (B). The spatial extend of the models approximates the maximum viewing area of AMSPEC (±150 m from center=tower). The line with higher elevations shown Figure 7A is due to a tram line which was installed at the site during the BOREAS field experiment. This area has been excluded from the analysis of α_s.

Figure 8: LiDAR derived viewshed model for θ_v=45˚ as observed at the SOA (Figure A) and DF-49 site (Figure B). The hillshade analysis was carried out only for those canopy areas visible from the tower. The ellipse shown in both figures represents an example of an area observed AMSPEC II at a given zenith and azimuth (here: θ_v=78˚ and ϕ_v=225˚). The relatively smooth canopy at the SOA site yields an almost complete observation of the canopy around the tower with α_s being relatively small (here <30%), where as α_s is much higher at DF-49.

Figure 9: Relationship between AMSPEC observed PRI and α_s observed during one 15-minute interval (Figure A: SOA, Figure B: DF-49). During this time period ε was assumed to be constant (ε=0.45 g CMJ^{-1} in both cases).

Figure 10: Relationship between ΔPRI Δαs-1 and EC-measured ε. The regression line established from DF49 data is solid; the one established from SOA data is dashed. The gray areas correspond to the 95% confidence interval around both regressions. Both regressions are falling within the 95% confidence interval of each other and both show a similar, logarithmic behaviour.

References

Asner, G. (1998). Biophysical and biochemical sources of variability in canopy reflectance. *Remote Sensing of Environment, 64*

Baldocchi, D.D. (2003). Assessing the Eddy Covariance Technique for Evaluating Carbon Dioxide Exchange Rates of Ecosystems: Past, Present and Future. *Global Change Biology, 9*, 479-492

Barr, A.G., Black, T.A., Hogg, E.H., Griffis, T.J., Morgenstern, K., Kljun, N., Theede, A., & Nesic, Z. (2007). Climatic controls on the carbon and water balances of a boreal aspen forest, 1994-2003. *Global Change Biology, 13*, 561-576

Barr, A.G., Black, T.A., Hogg, E.H., Kljun, N., Morgenstern, K., & Nesic, Z. (2004). Inter-annual variability in the leaf area index of a boreal aspen-hazelnut forest in relation to net ecosystem production. *Agricultural and Forest Meteorology, 126*, 237-255

Barton, C.V.M., & North, P.R.J. (2001). Remote Sensing of Canopy Light Use Efficiency Using the Photochemical Reflectance Index - Model and Sensitivity Analysis. *Remote Sensing of Environment, 78*, 264-273

Chen, J.M. (1996). Canopy Architecture and Remote Sensing of the Fraction of Photosynthetically Active Radiation Absorbed by Boreal Conifer Forests. *Ieee Transactions on Geoscience and Remote Sensing, 34*, 1353-1368

Chen, J.M., Govind, A., Sonnentag, O., Zhang, Y.Q., Barr, A., & Amiro, B.D. (2006). Leaf Area Index Measurements at Fluxnet-Canada Forest Sites. *Agricultural and Forest Meteorology, 140*, 257-268

Chen, J.M., Liu, J., Leblanc, S.G., Lacaze, R., & Roujean, J.L. (2003). Multi-angular optical remote sensing for assessing vegetation structure and carbon absorption. *Remote Sensing of Environment, 84*, 516-525

Coops, N.C., Hilker, T., Wulder, M.A., St-Onge, B., Newnham, G., Siggins, A., & Trofymow, J.A. (2007). Estimating canopy structure of Douglas-fir forest stands from discrete-return LiDAR. *Trees-Structure and Function, 21*, 295-310

Crawford, P.S., Brooks, A.R., & Brush, R.J.H. (1996). Fast navigation of AVHRR images using complex orbital models. *International Journal of Remote Sensing, 17*, 197-212

Demmig- Adams, B., & Adams, W.W. (1996). The Role of Xanthophyll Cycle Carotenoids in the Protection of Photosynthesis. *Trends in Plant Science, 1*, 21-26

Drolet, G.G., Huemmrich, K.F., Hall, F.G., Middleton, E.M., Black, T.A., Barr, A.G., & Margolis, H.A. (2005). A Modis-Derived Photochemical Reflectance Index to Detect Inter-Annual Variations in the Photosynthetic Light-Use Efficiency of a Boreal Deciduous Forest. *Remote Sensing of Environment, 98*, 212-224

Drolet, G.G., Middleton, E.M., Huemmrich, K.F., Hall, F.G., Amiro, B.D., Barr, A.G., Black, T.A., mcCaughey, H.A., & Margolis, H.A. (2008). Regional mapping of gross light-use efficiency using MODIS spectral indices. *Remote Sensing of Environment, 112*, 3064-3078

Field, C., & Mooney, H.A. (1986). THE PHOTOSYNTHESIS-NITROGEN RELATIONSHIP IN WILD PLANTS. *Givnish, T. J. (Ed.). on the Economy of Plant Form and Function; Sixth Maria Moors Cabot Symposium on Evolutionary Constraints on Primary Productivity: Adaptive Patterns of Energy Capture in Plants, Harvard Forest, Mass., USA, Aug. 6, 1983. Xvii+717p. Cambridge University Press: New York, N.Y., USA: Cambridge, England. Illus*, 25-56

Filella, I., Amaro, T., Araus, J.L., & Penuelas, J. (1996). Relationship Between Photosynthetic Radiation-Use Efficiency of Barley Canopies and the Photochemical Reflectance Index (Pri). *Physiologia Plantarum, 96*, 211-216

Gamon, J.A., Filella, I., & Penuelas, J. (Eds.) (1993). *The dynamic 531-nanometer reflectance signal: A survey of twenty angiosperm species*: American Society of Plant Physiologists: Rockville.

Gamon, J.A., Penuelas, J., & Field, C.B. (1992). A Narrow-Waveband Spectral Index That Tracks Diurnal Changes in Photosynthetic Efficiency. *Remote Sensing of Environment, 41*, 35-44

Gamon, J.A., Serrano, L., & Surfus, J.S. (1997). The Photochemical Reflectance Index: an Optical Indicator of Photosynthetic Radiation Use Efficiency Across Species, Functional Types, and Nutrient Levels. *Oecologia, 112*, 492-501

Gamon, P.F. (1992). A Narrow-Waveband Spectral Index That Tracks Diurnal Changes in Photosynthetic Efficiency. *Remote sensing of environment, 41:*, 35-44

Garbulsky, M.F., Penuelas, J., Papale, D., & Filella, I. (2008). Remote estimation of carbon dioxide uptake by a Mediterranean forest. *Global Change Biology, 14*, 2860-2867

Goerner, A., Reichstein, M., & Rambal, S. (2009). Tracking seasonal drought effects on ecosystem light use efficiency with satellite-based PRI in a Mediterranean forest. *Remote Sensing of Environment, 113*, 1101-1111

Griffis, T.J., Black, T.A., Gaumont-Guay, D., Drewitt, G.B., Nesic, Z., Barr, A.G., Morgenstern, K., & Kljun, N. (2004). Seasonal Variation and Partitioning of Ecosystem Respiration in a Southern Boreal Aspen Forest. *Agricultural and Forest Meteorology, 125*, 207-223

Hais, M., & Kucera, T. (2009). The influence of topography on the forest surface temperature retrieved from Landsat TM, ETM plus and ASTER thermal channels. *Isprs Journal of Photogrammetry and Remote Sensing, 64*, 585-591

Hall, F.G., Hilker, T., Coops, N.C., Lyapustin, A., Huemmrich, K.F., Middleton, E., Margolis, H., Drolet, G., & Black, T.A. (2008). Multi-angle remote sensing of forest light use efficiency by observing PRI variation with canopy shadow fraction. *Remote Sensing of Environment, 112*, 3201-3211

Hall, S., Burke, I., Box, D., Kaufmann, M., & Stoker, J. (2005). Estimating stand structure using discrete-return lidar: an example from low density, fire prone ponderosa pine forets. *Forest Ecology and Management, 208*, 189-209

Hilker, T., Coops, N.C., Coggins, S.B., Wulder, M.A., Brown, M., Black, T.A., Nesic, Z., & Lessard, D. (2009a). Detection of foliage conditions and disturbance from multi-angular high spectral resolution remote sensing. *Remote Sensing of Environment, 113*, 421-434

Hilker, T., Coops, N.C., Hall, F.G., Black, T.A., Wulder, M.A., Nesic, Z., & Krishnan, P. (2008a). Separating physiologically and directionally induced changes in PRI using BRDF models. *Remote Sensing of Environment, 112*, 2777-2788

Hilker, T., Coops, N.C., Nesic, Z., Wulder, M.A., & Black, A.T. (2007). Instrumentation and approach for unattended year round tower based measurements of spectral reflectance. *Computers and Electronics in Agriculture, 56*, 72-84

Hilker, T., Coops, N.C., Schwalm, C.R., Jassal, R.S., Black, T.A., & Krishnan, P. (2008b). Effects of mutual shading of tree crowns on prediction of photosynthetic light-use efficiency in a coastal Douglas-fir forest. *Tree Physiology, 28*, 825-834

Hilker, T., Lyapustin, A., Hall, F.G., Wang, Y., Coops, N.C., Drolet, G., & Black, T.A. (2009b). An assessment of photosynthetic light use efficiency from space: Modeling the atmospheric and directional impacts on PRI reflectance. *Remote Sensing of Environment, 113*, 2463-2475

Hilker, T., Nesic, Z., Coops, Nicholas C., & Lessard, D. (submitted). A new automated multi-angular radiometer instrument for tower based observations of canopy reflectance (Amspec II). *Computers and Electronics in Agriculture*

Humphreys, E.R., Black, T.A., Morgenstern, K., Cai, T.B., Drewitt, G.B., Nesic, Z., & Trofymow, J.A. (2006). Carbon Dioxide Fluxes in Coastal Douglas-Fir Stands at Different Stages of Development After Clearcut Harvesting. *Agricultural and Forest Meteorology, 140*, 6-22

Jassal, R.S., Black, T.A., Cai, T.B., Morgenstern, K., Li, Z., Gaumont-Guay, D., & Nesic, Z. (2007). Components of Ecosystem Respiration and an Estimate of Net Primary Productivity of an Intermediate-Aged Douglas-Fir Stand. *Agricultural and Forest Meteorology, 144*, 44-57

Kelso, T.S. (2007). Validation of SGP4 and IS-GPS-200D against GPS precision ephemerides. In M.R. Akella, J.W. Gearhart, R.H. Bishop & A.J. Treder (Eds.), *AAS/AIAA 17th Space Flight Mechanics Meeting* (pp. 427-440). Sedona, AZ: Amer Astronautical Soc

Kim, Y.H., Rana, S., & Wise, S. (2004). Exploring multiple viewshed analysis using terrain features and optimisation techniques. *Computers & Geosciences, 30*, 1019-1032

Kodani, E., Awaya, Y., Tanaka, K., & Matsumura, N. (2002). Seasonal patterns of canopy structure, biochemistry and spectral reflectance in a broad-leaved deciduous Fagus crenata canopy. *Forest Ecology and Management, 167*, 233-249

Li, X., & Strahler, A. (1985). Geometric-optical modeling of a conifer forest canopy. *IEEE Transactions on Geoscience and Remote Sensing, GE-23*, 705-721

Lyapustin, A., & Wang, Y. (2009). *The time series technique for aerosol retrievals overland from MODIS*. Berlin: Springer Praxis Books978-3-540-69396-3.

Lyapustin, A., & Wang, Y.J. (2005). Parameterized code SHARM-3D for radiative transfer over inhomogeneous surfaces. *Applied Optics, 44*, 7602-7610

Lyapustin, A.I. (2005). Radiative transfer code SHARM for atmospheric and terrestrial applications. *Applied Optics, 44*, 7764-7772

Margolis, H.A., Flanagan, L.B., & Amiro, B.D. (2006). The Fluxnet-Canada Research Network: Influence of climate and disturbance on carbon cycling in forests and peatlands. *Agricultural and Forest Meteorology, 140*, 1-5

Middleton, E.M., Cheng, Y.B., Hilker, T., Black, T.A., Krishnan, P., Coops, N.C., & Huemmrich, K.F. (2009). Linking foliage spectral responses to canopy-level ecosystem photosynthetic light-use efficiency at a Douglas-fir forest in Canada. *Canadian Journal of Remote Sensing, 35*, 166-188

Monteith, J.L. (1972). Solar-Radiation and Productivity in Tropical Ecosystems. *Journal of Applied Ecology, 9*, 747-766

Monteith, J.L. (1977). Climate and Efficiency of Crop Production in Britain. *Philosophical Transactions of the Royal Society of London Series B-Biological Sciences, 281*, 277-294

Morgenstern, K., Black, T.A., Humphreys, E.R., Griffis, T.J., Drewitt, G.B., Cai, T.B., Nesic, Z., Spittlehouse, D.L., & Livingstone, N.J. (2004). Sensitivity and Uncertainty of the Carbon Balance of a Pacific Northwest Douglas-Fir Forest During an El Nino La Nina Cycle. *Agricultural and Forest Meteorology, 123*, 201-219

Nichol, C.J., Huemmrich, K.F., Black, T.A., Jarvis, P.G., Walthall, C.L., Grace, J., & Hall, F.G. (2000). Remote Sensing of Photosynthetic-Light-Use Efficiency of Boreal Forest. *Agricultural and Forest Meteorology, 101*, 131-142

Penuelas, J., Filella, I., & Gamon, J.A. (1995). Assessment of Photosynthetic Radiation-Use Efficiency With Spectral Reflectance. *New Phytologist, 131*, 291-296

Penuelas, J., Filella, I., Gamon, J.A., & Field, C. (1997). Assessing Photosynthetic Radiation-Use Efficiency of Emergent Aquatic Vegetation From Spectral Reflectance. *Aquatic Botany, 58*, 307-315

Reichstein, M., Papale, D., Valentini, R., Aubinet, M., Bernhofer, C., Knohl, A., Laurila, T., Lindroth, A., Moors, E., Pilegaard, K., & Seufert, G. (2007). Determinants of terrestrial ecosystem carbon balance inferred from European eddy covariance flux sites. *Geophysical Research Letters, 34*

Richardson, A.D., Hollinger, D.Y., Dail, D.B., Lee, J.T., Munger, J.W., & O'Keefe, J. (2009). Influence of spring phenology on seasonal and annual carbon balance in two contrasting New England forests. *Tree Physiology, 29*, 321-331

Richardson, A.D., Jenkins, J.P., Braswell, B.H., Hollinger, D.Y., Ollinger, S.V., & Smith, M.L. (2007). Use of digital webcam images to track spring green-up in a deciduous broadleaf forest. *Oecologia, 152*, 323-334

Ross, J.K. (1981). *The radiation regime and architecture of plant stands*. The Hague: Dr. W. Junk Publishers

Roujean, J.L., Leroy, M., & Deschamps, P.Y. (1992). A Bidirectional Reflectance Model of the Earths Surface for the Correction of Remote-Sensing Data. *Journal of Geophysical Research-Atmospheres, 97*, 20455-20468

Sims, D.A., & Gamon, J.A. (2002). Relationships Between Leaf Pigment Content and Spectral Reflectance Across a Wide Range of Species, Leaf Structures and Developmental Stages. *Remote Sensing of Environment, 81*, 337-354

Tan, B., Woodcock, C.E., Hu, J., Zhang, P., Ozdogan, M., Huang, D., Yang, W., Knyazikhin, Y., & Myneni, R.B. (2006). The impact of gridding artifacts on the local spatial properties of MODIS data: Implications for validation, compositing, and band-to-band registration across resolutions. *Remote Sensing of Environment, 105*, 98-114

Vermote, E.F., & Kotchenova, S. (2008). Atmospheric correction for the monitoring of land surfaces. *Journal of Geophysical Research-Atmospheres, 113*

Vermote, E.F., Tanre, D., Deuze, J.L., Herman, M., & Morcrette, J.J. (1997). Second Simulation of the Satellite Signal in the Solar Spectrum, 6S: An overview. *Ieee Transactions on Geoscience and Remote Sensing, 35*, 675-686

Wolfe, R.E., Roy, D.P., & Vermote, E. (1998). MODIS land data storage, gridding, and compositing methodology: Level 2 grid. *Ieee Transactions on Geoscience and Remote Sensing, 36*, 1324-1338

Figure 1
Click here to download high resolution image

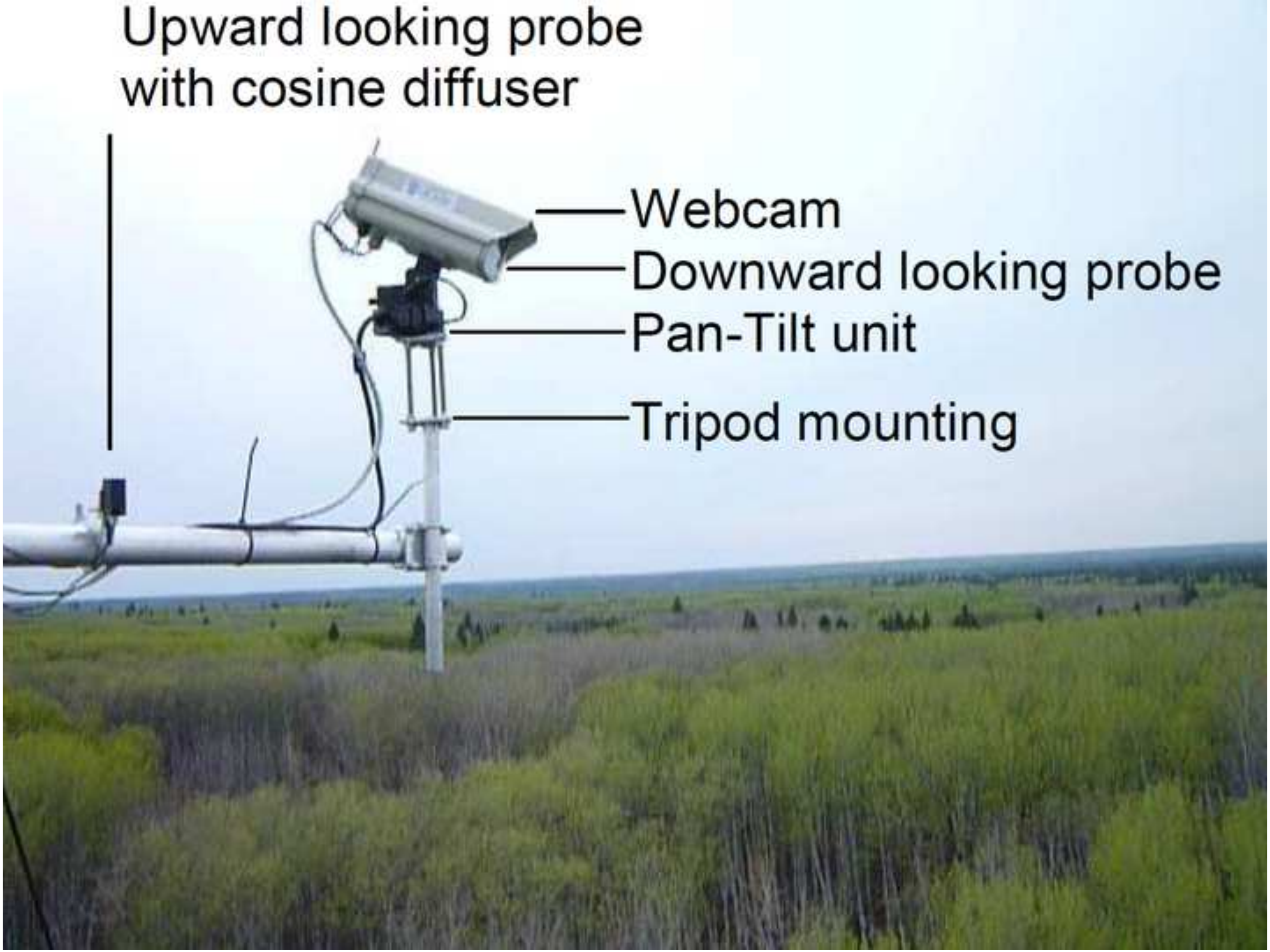

Figure 2
Click here to download high resolution image

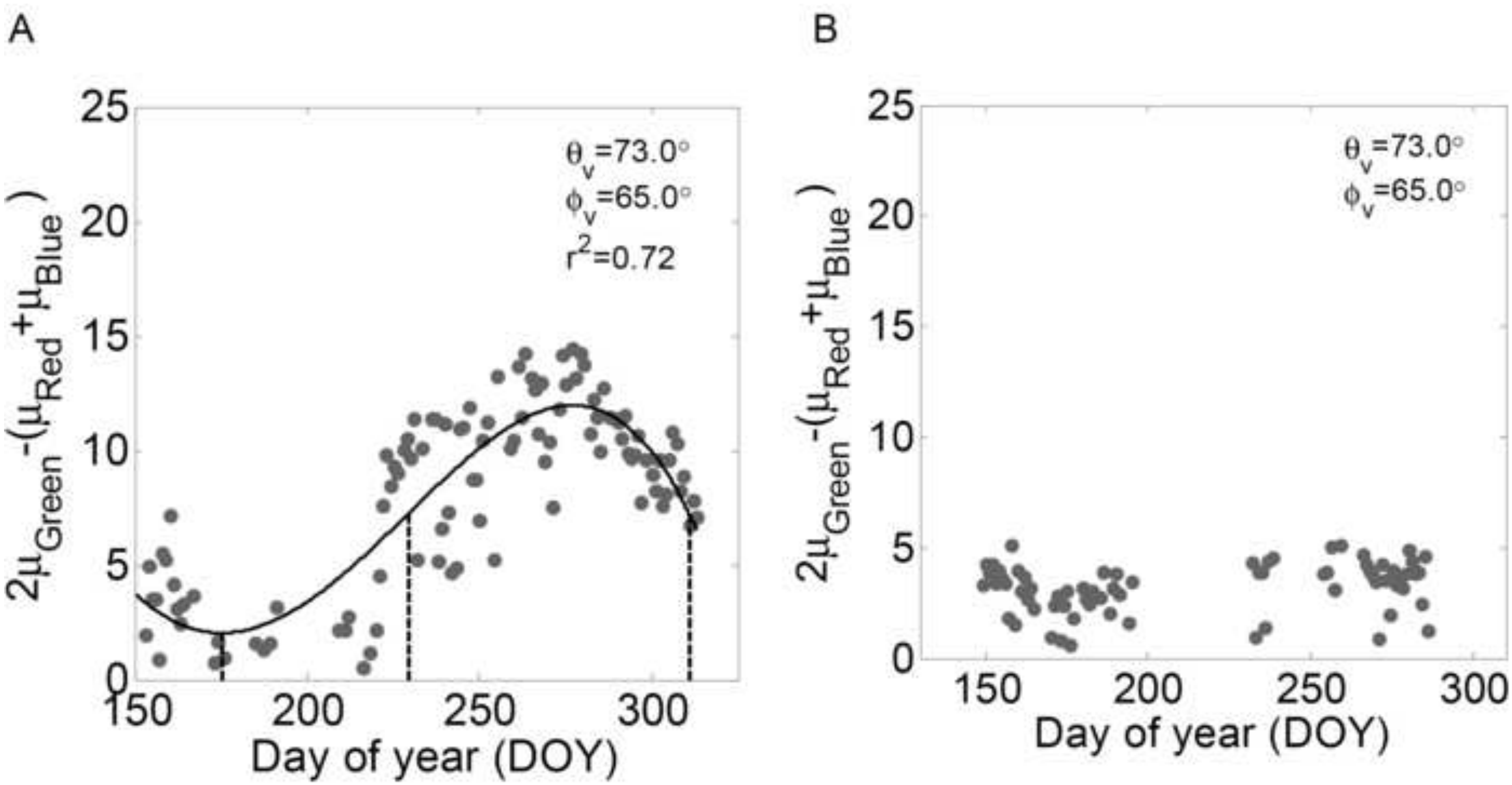

Figure 3

Click here to download high resolution image

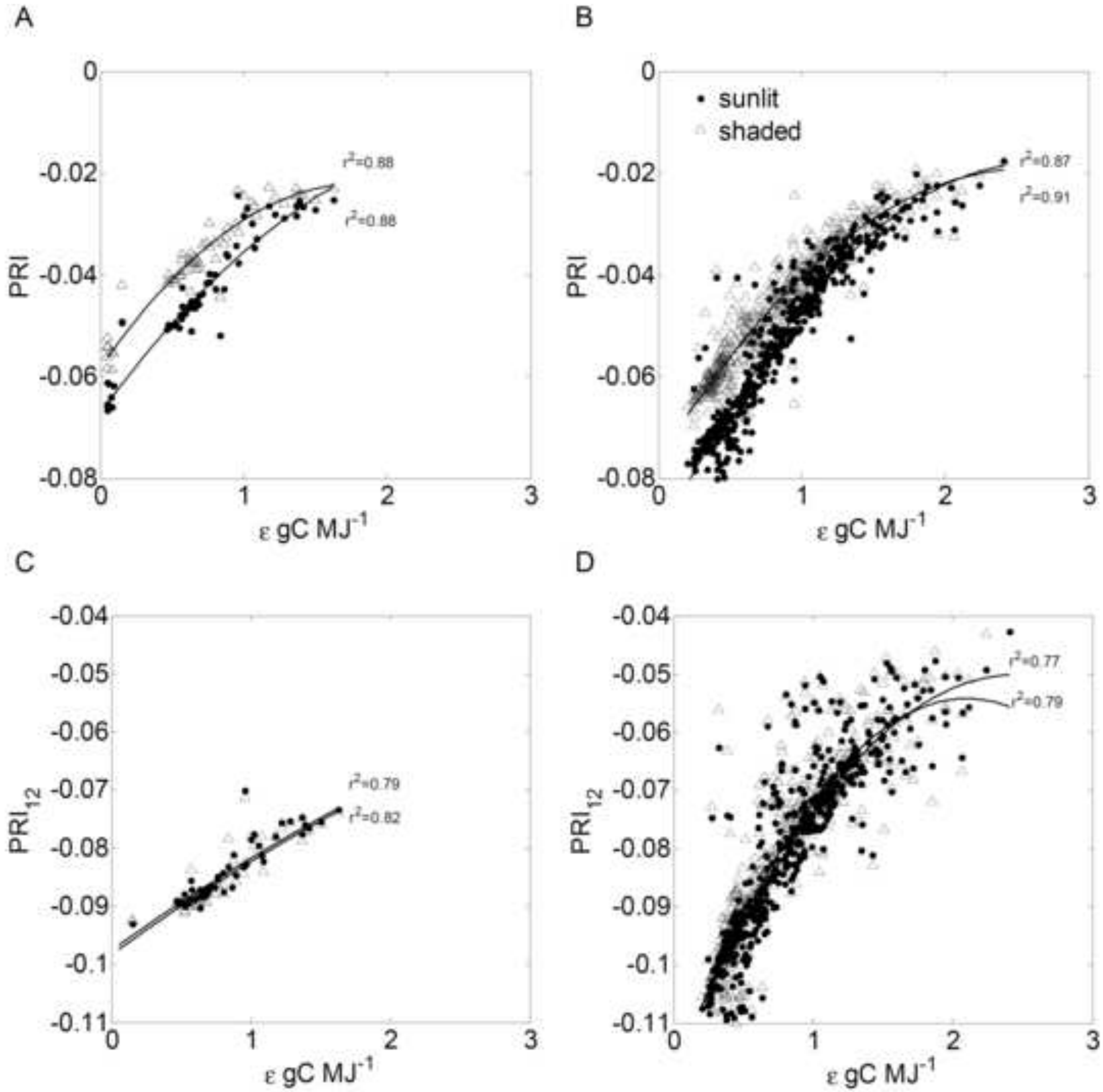

Figure 4

Click here to download high resolution image

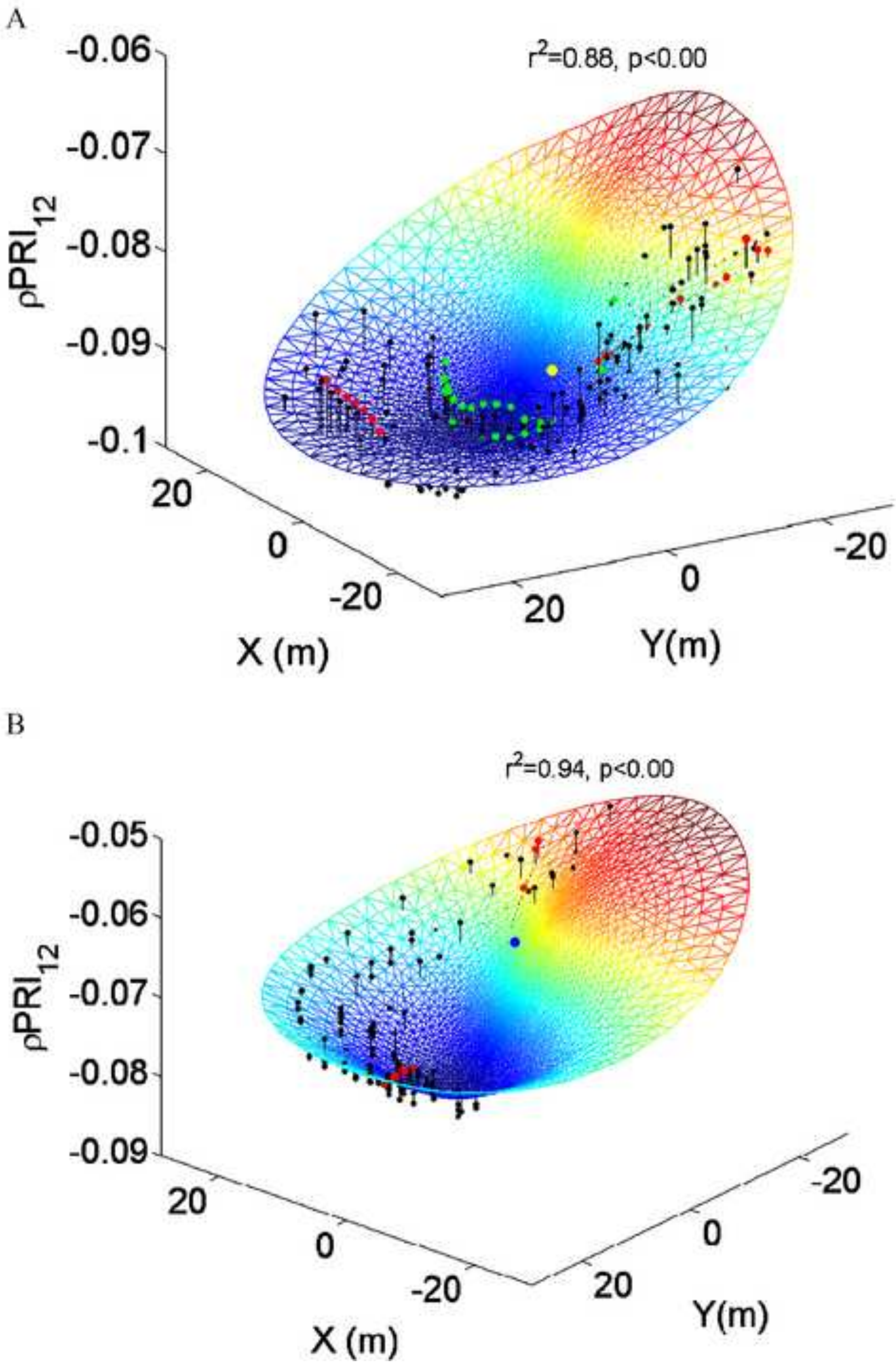

Figure 5
Click here to download high resolution image

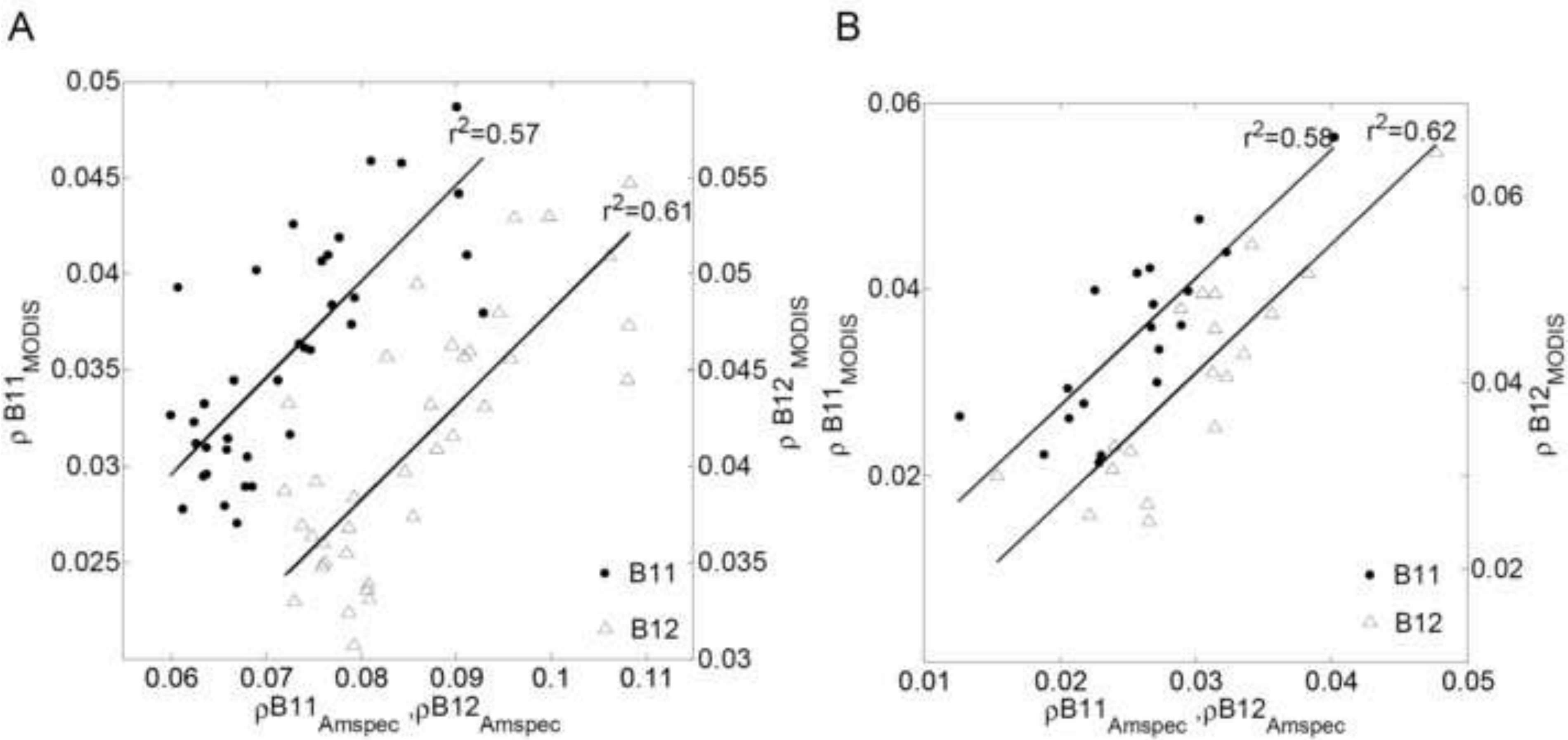

Figure 6
Click here to download high resolution image

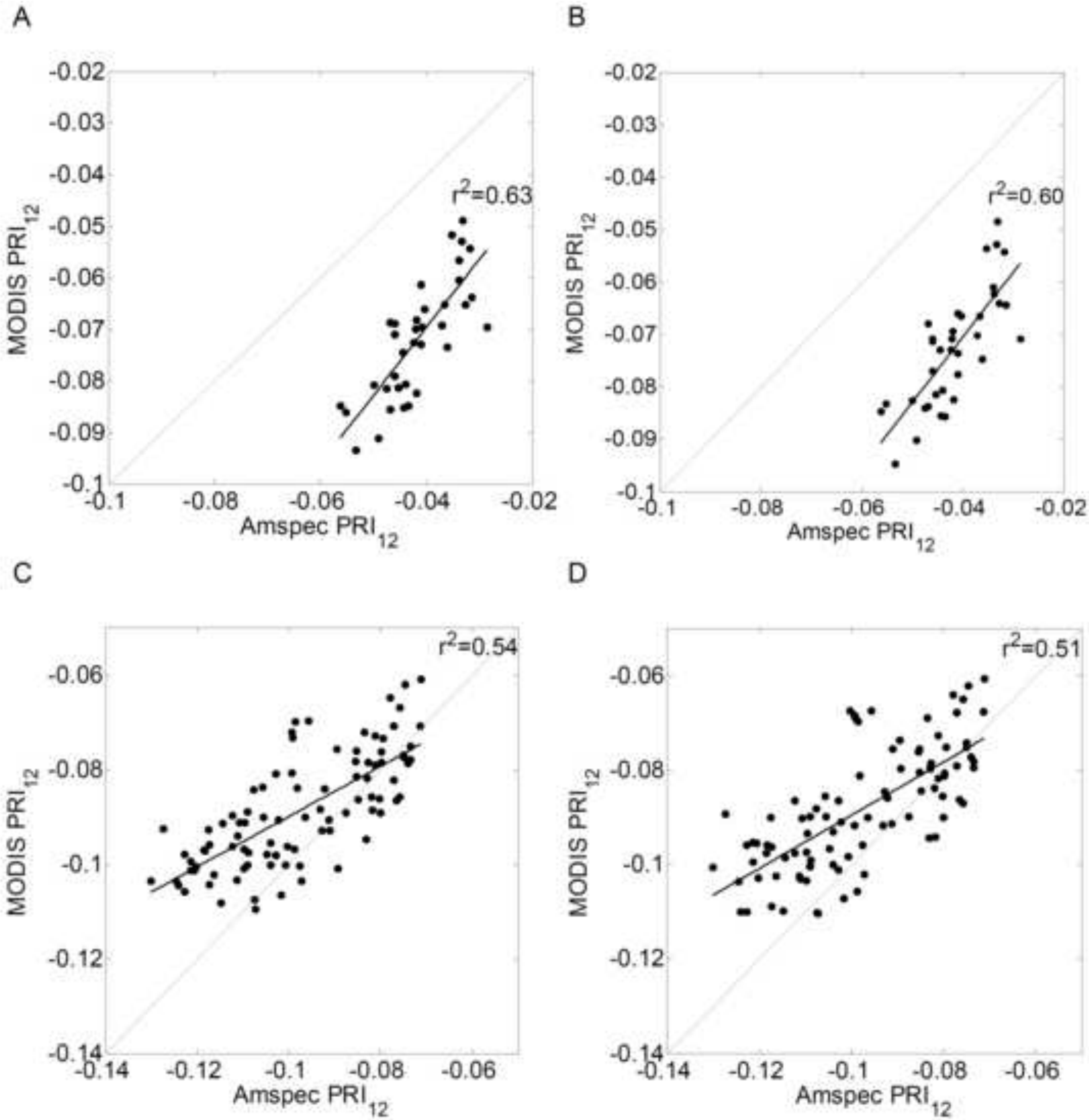

Figure 7

Click here to download high resolution image

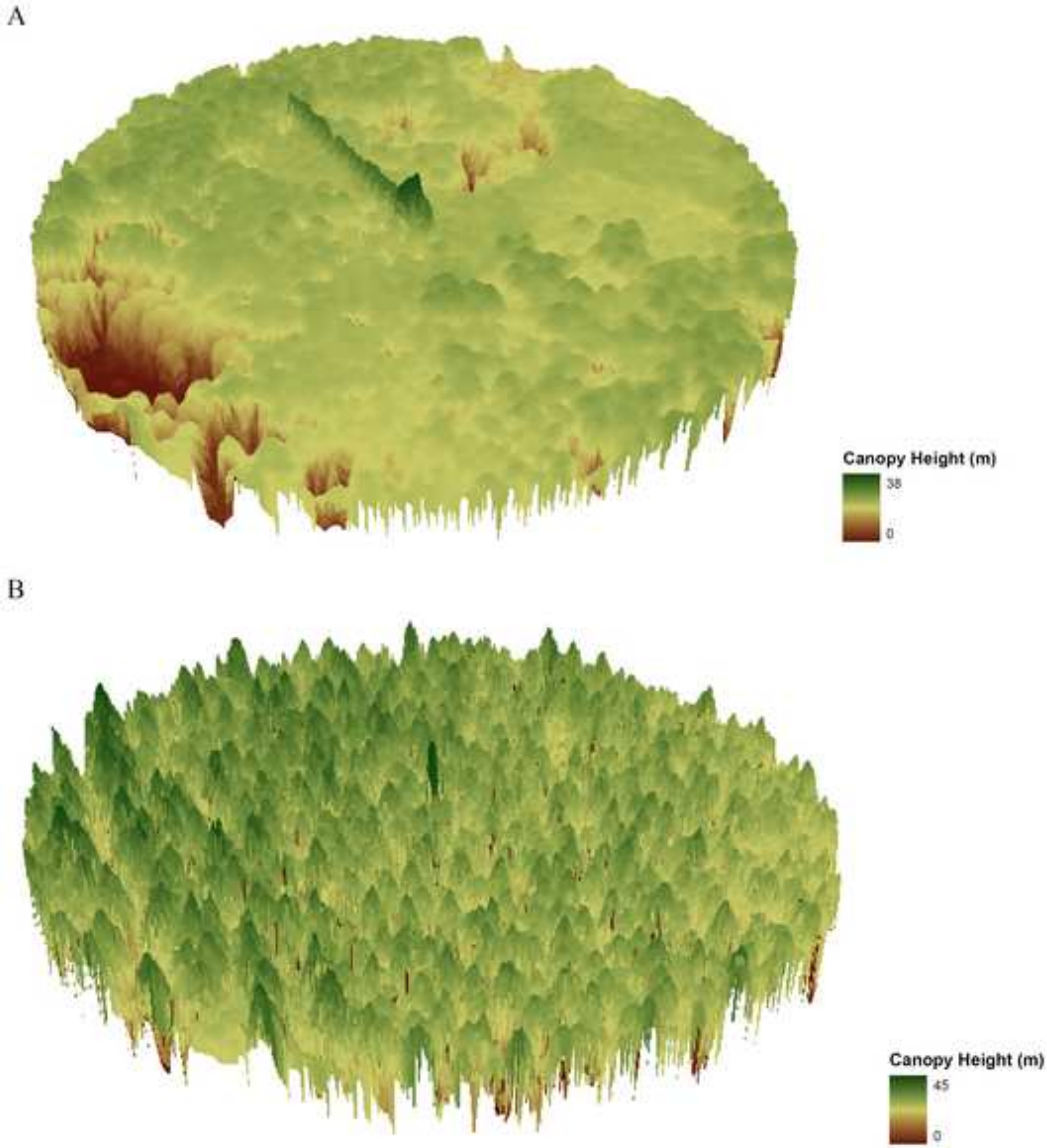

Figure 8

Click here to download high resolution image

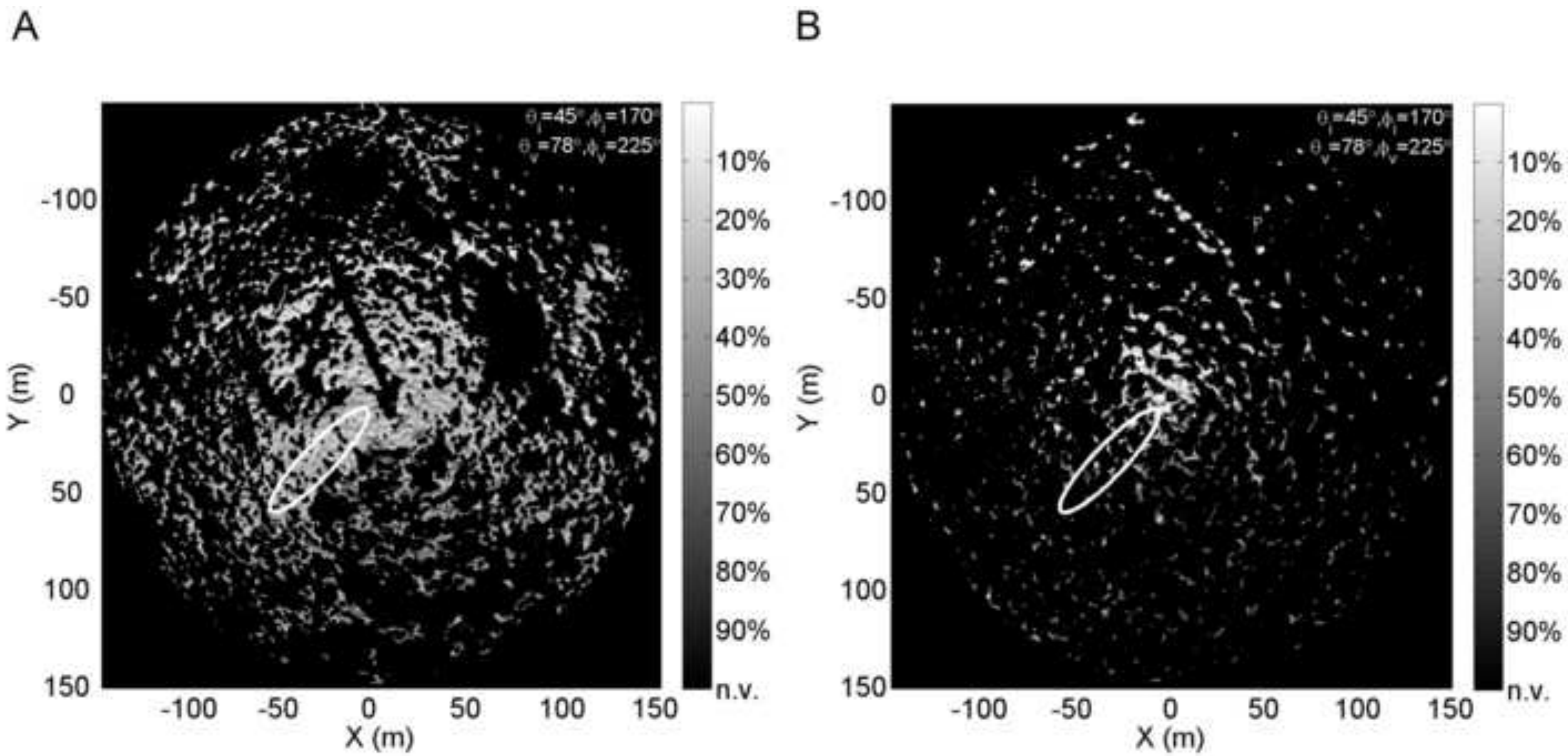

Figure 9
Click here to download high resolution image

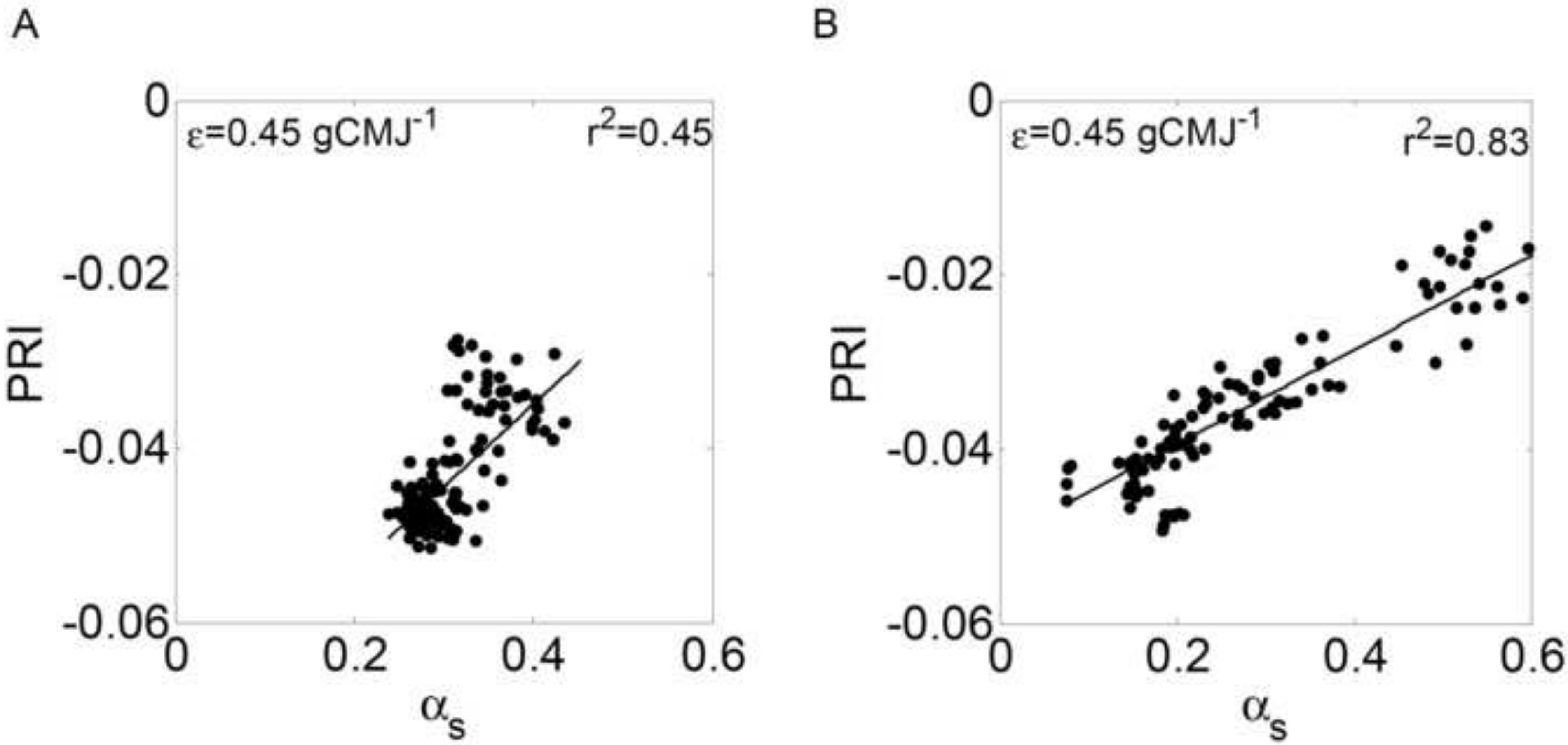

Figure 10
Click here to download high resolution image